PHYSICAL REVIEW B **77**, 205112 (2008)

Plane-wave based electronic structure calculations for correlated materials using dynamical mean-field theory and projected local orbitals

B. Amadon,[1] F. Lechermann,[2] A. Georges,[3] F. Jollet,[1] T. O. Wehling,[2] and A. I. Lichtenstein[2]

[1]*Département de Physique Théorique et Appliquée, CEA, Bruyères-le-Châtel, 91297 Arpajon, Cedex, France*
[2]*I. Institut für Theoretische Physik, Universität Hamburg, D-20355 Hamburg, Germany*
[3]*Centre de Physique Théorique, École Polytechnique, 91128 Palaiseau, Cedex, France*

(Received 28 January 2008; revised manuscript received 15 April 2008; published 15 May 2008)

The description of realistic strongly correlated systems has recently advanced through the combination of density functional theory in the local density approximation (LDA) and dynamical mean field theory (DMFT). This LDA+DMFT method is able to treat both strongly correlated insulators and metals. Several interfaces between LDA and DMFT have been used, such as (*N*th order) linear muffin-tin orbitals or maximally localized Wannier functions. Such schemes are, however, either complex in use or additional simplifications are often performed (i.e., the atomic sphere approximation). We present an alternative implementation of LDA+DMFT, which keeps the precision of the Wannier implementation, but which is lighter. It relies on the projection of localized orbitals onto a restricted set of Kohn–Sham states to define the correlated subspace. The method is implemented within the projector augmented wave and within the mixed-basis pseudopotential frameworks. This opens the way to electronic structure calculations within LDA+DMFT for more complex structures with the precision of an all-electron method. We present an application to two correlated systems, namely, $SrVO_3$ and β-NiS (a charge-transfer material), including ligand states in the basis set. The results are compared to calculations done with maximally localized Wannier functions, and the physical features appearing in the orbitally resolved spectral functions are discussed.

DOI: 10.1103/PhysRevB.77.205112 PACS number(s): 71.10.Fd, 71.30.+h, 71.15.Ap, 71.15.Mb

I. INTRODUCTION

The description of strong electronic correlations in a realistic framework has become an issue of major importance in current condensed matter research. Due to the fast progress in the preparation of novel materials, especially in effectively reduced dimensions, and the advances in experimental techniques in order to probe such systems, providing an adequate theoretical formalism that can handle explicit many-body effects in a material-specific context is crucial. It is evident that standard density functional theory (DFT) in the local density approximation (LDA) cannot meet those demands and, at least, has to ally with manifest many-body techniques. In this respect, the combination of DFT-LDA with the dynamical mean-field theory (DMFT), the so-called LDA+DMFT approach, has proven to be an invaluable method to face the challenge. Already numerous studies within the LDA+DMFT framework have shown that this theory is capable of describing the effects of strong correlations in a realistic context, such as Mott transitions and volume-collapse transitions in *d*- and *f*-electron systems, effective mass enhancement, local moment formation and magnetism, spectral-weight transfers, orbital physics, etc.

In view of these successes, it is crucial to push further the range of applicability of LDA+DMFT methods. To this aim, implementing LDA+DMFT within those electronic structure methods, which are highly accurate and allow for the possible treatment of larger systems, is certainly an important endeavor. One of the main aims of this paper is to report on such implementations, within a projector augmented wave (PAW) and a mixed-basis pseudopotential (MBPP) method. The formalism used in this paper is actually quite general and allows for an implementation of LDA+DMFT in a very large class of electronic structure methods. We present this formalism in an arbitrary basis set, which should make this task easier for other implementations. However, in our specific implementation, we make an extensive use of the Bloch basis set of Kohn–Sham (KS) orbitals. In order to implement LDA+DMFT, we use local orbitals constructed by projecting atomiclike orbitals onto a restricted set of Bloch states, a strategy similar to that introduced by Anisimov *et al.*[1]

Another important route is to investigate how to optimize the application of LDA+DMFT for a specific material, or class of materials of interest. Indeed, it is important to realize that, while the results of course do not depend on the specific basis set used in the calculation, they will actually depend on the specific set of *local orbitals* for which many-body effects will be taken into account, or more precisely (following the terminology introduced in Ref. 2) on the "correlated" subspace $\mathcal{C}$ of the full Hilbert space spanned by these orbitals. Indeed, the DMFT treatment applies local interaction terms to those orbitals only, and furthermore neglects all nonlocal components of the self-energy. This notion of locality is defined with respect to the specific choice of the local orbitals defining $\mathcal{C}$, and the accuracy of the DMFT approximation cannot be expected to be identical for different choices.

Early implementations[3–5] of LDA+DMFT used the linear muffin-tin orbital[6] (LMTO) framework, and the correlated orbitals were frequently identified with a specific subset of the LMTO basis functions, having *d* or *f* character. There is no specific reason to pick the local orbitals as members of the basis set, however, and a set of atomiclike functions may prove to be better from the physical point of view. Recently, several works have used different kinds of Wannier functions (WFs) as correlated orbitals, starting with the work of Pavarini *et al.*[7] using *N*th-order muffin-tin orbitals[8] (NMTO).

©2008 The American Physical Society

Anisimov *et al.*[1] used WFs constructed from a projection on a subset of the Bloch functions,[9,10] and Lechermann *et al.* used maximally localized[11] WFs (MLWFs) and compared the results to those using NMTOs.

The energy window spanned by the basis functions that are retained in the implementation, and the spatial extension of the local orbitals defining $\mathcal{C}$ are important physical issues for the description of a given material. Those issues become particularly important for charge-transfer materials (e.g., late transition-metal oxides, sulfides, or selenides) in which the ligand states must be kept in the basis set in order to reach a satisfactory physical picture. In this paper, we address these issues and provide explicit comparisons between calculations performed with more spatially extended local orbitals (hence, spanning a smaller energy window when projected onto Bloch functions) and more localized local orbitals (hence, spanning a wider energy window).

This paper is organized as follows. Section II is devoted to a presentation of the general theoretical framework. Sections III and IV are devoted to applications to two compounds, which are considered as tests for the method: the transition-metal oxide $\mathrm{SrVO_3}$ in Sec. III and the charge-transfer sulfide NiS in Sec. IV.

II. THEORETICAL FRAMEWORK

A. LDA+DMFT formalism in an arbitrary basis set

In order to implement DMFT within realistic electronic structure calculations of correlated-electron materials, one has to set up a formalism, which keeps track of the real-space (i.e., quantum chemical) and the reciprocal-space (i.e., solid-state) aspects on an equal footing, while being computationally efficient. Following the work of Lechermann *et al.*,[2] we therefore distinguish between the complete basis set $\{|B_{\mathbf{k}\alpha}\rangle\}$ in which the full electronic structure problem on a lattice is formulated (and accordingly the lattice Green's function is represented), and local orbitals $|\chi_m^{\mathbf{R}}\rangle$, which span a correlated subspace $\mathcal{C}$ of the total Hilbert space. Many-body corrections beyond LDA will be considered inside this subspace. The index α labels the basis functions for each wave vector $\mathbf{k}$ in the Brillouin zone. The index $\mathbf{R}$ denotes the correlated atom within the primitive unit cell, around which the local orbital $|\chi_m^{\mathbf{R}}\rangle$ is centered, and $m=1,\ldots,M$ is an orbital index within the correlated subset. Projection on that subset, for atom type $\mathbf{R}$, is done with the following projection operator:

$$\hat{P}_{\mathbf{R}}^{(\mathcal{C})} \equiv \sum_{m\in\mathcal{C}} |\chi_m^{\mathbf{R}}\rangle\langle\chi_m^{\mathbf{R}}|. \qquad (1)$$

In Ref. 2, it was shown that the DMFT self-consistency condition, which relates the impurity Green's function $\mathbf{G}_{\mathrm{imp}}^{\mathbf{R}}$ to the Green's function of the solid locally computed on atom $\mathbf{R}$, reads

$$G_{mm'}^{\mathrm{R},imp}(i\omega_n) = \sum_{\mathbf{k}} \sum_{\alpha\alpha'} \langle\chi_{\mathbf{k}m}^{\mathbf{R}}|B_{\mathbf{k}\alpha}\rangle\langle B_{\mathbf{k}\alpha'}|\chi_{\mathbf{k}m'}^{\mathbf{R}}\rangle \times\{[i\omega_n+\mu-\mathbf{H}_{\mathrm{KS}}(\mathbf{k})-\Delta\Sigma(\mathbf{k},i\omega_n)]^{-1}\}_{\alpha\alpha'}. \qquad (2)$$

In this expression,

$$|\chi_{\mathbf{k}m}^{\mathbf{R}}\rangle = \sum_{\mathbf{T}} \mathrm{e}^{i\mathbf{k}\cdot(\mathbf{T}+\mathbf{R})}|\chi_{\mathbf{T}m}^{\mathbf{R}}\rangle \qquad (3)$$

denotes the Bloch transform of the local orbitals whereby $\mathbf{T}$ denotes the Bravais lattice translation vectors. Note that the object in the second line of Eq. (2) is, of course, nothing else than the full lattice Green's function $G_{\alpha\alpha'}(\mathbf{k},i\omega_n)$ in the chosen $\{|B_{\mathbf{k}\alpha}\rangle\}$ basis. The KS Hamiltonian $\mathbf{H}_{\mathrm{KS}}(\mathbf{k})$ is obtained by solving the Kohn–Sham equations, which yield eigenvalues $\varepsilon_{\mathbf{k}\nu}$ and Bloch wave functions $|\Psi_{\mathbf{k}\nu}\rangle$ (ν is the band index). It can be expressed in the $\{|B_{\mathbf{k}\alpha}\rangle\}$ basis set as

$$\mathbf{H}_{\mathrm{KS},\alpha\alpha'}(\mathbf{k}) = \sum_{\nu} \langle B_{\mathbf{k}\alpha}|\Psi_{\mathbf{k}\nu}\rangle\varepsilon_{\mathbf{k}\nu}\langle\Psi_{\mathbf{k}\nu}|B_{\mathbf{k}\alpha'}\rangle. \qquad (4)$$

In order to obtain the self-energy for the full solid, one has to promote ("upfold") the DMFT impurity self-energy $\Sigma_{mm'}^{\mathrm{imp}}$ to the lattice via[2]

$$\Delta\Sigma_{\alpha\alpha'}(\mathbf{k},i\omega_n) = \sum_{\mathbf{R}} \sum_{mm'} \langle B_{\mathbf{k}\alpha}|\chi_{\mathbf{k}m}^{\mathbf{R}}\rangle\langle\chi_{\mathbf{k}m'}^{\mathbf{R}}|B_{\mathbf{k}\alpha'}\rangle[\Sigma_{mm'}^{\mathrm{imp}}(i\omega_n) - \Sigma_{mm'}^{\mathrm{dc}}], \qquad (5)$$

whereby a double-counting correction $\Sigma_{mm'}^{\mathrm{dc}}$, which takes care of correlation effects already accounted for in the LDA Hamiltonian (see Appendix B), has to be included in the general case.

The above equations form the general LDA+DMFT framework, in a general arbitrary basis set. Any specific implementation must then make a choice for the following: (i) the set of local orbitals $\{|\chi_m^{\mathbf{R}}\rangle\}$ spanning the correlated subspace and (ii) the specific basis set $\{|B_{\mathbf{k}\alpha}\rangle\}$ in which these equations will be implemented.

It is important to realize that the results will certainly depend on the specific choice of $\{|\chi_m^{\mathbf{R}}\rangle\}$: The quality of the DMFT approximation will indeed depend on how the local orbitals are picked such as to minimize nonlocal contributions. In contrast, for a given choice of $\{|\chi_m^{\mathbf{R}}\rangle\}$'s, the results should be, in principle, independent of the basis set $\{|B_{\mathbf{k}\alpha}\rangle\}$, which is chosen for the implementation. However, in practice, considerations of numerical efficiency do limit the size of the basis, which can be handled. Indeed, Eq. (2) involves inverting a matrix (at each $\mathbf{k}$ point and for each frequency) of size $N_b\times N_b$, in which N_b is the number of basis functions, which are eventually retained. Hence, in practice, one will restrict the basis set to a certain set $\mathcal{W}$ of bands, as will be described in more detail below. Regarding the choice of local orbitals, we recall that, in Ref. 2, different kinds of Wannier functions were used and compared to one another, namely, maximally localized Wannier functions[11] and NMTO.[8] The construction of such functions requires rather sophisticated procedures. In the present work, we use a somewhat lighter implementation, with the same demands on accuracy, by constructing the $\{|\chi_m^{\mathbf{R}}\rangle\}$'s out of entities that are already existing in most of the common band-structure codes, namely, using the decomposition of local atomiclike orbitals onto the basis function retained in the set $\mathcal{W}$. This is very similar in spirit to the construction proposed by Anisimov *et al.*[1] in the LMTO framework. The present construction, and the basic equations developed in this section, are fairly general, however, and can be implemented in an arbitrary electronic structure code.

B. LDA+DMFT formalism in the Bloch basis set

In this section, we focus on a very simple choice for the basis set, namely, the Bloch basis itself $\{|B_{\mathbf{k}\alpha}\rangle\}=\{|\Psi_{\mathbf{k}\nu}\rangle\}$. This basis is most conveniently used, since it is a direct output of any DFT-LDA calculation and furthermore diagonalizes the KS Hamiltonian $\mathbf{H}^{\text{KS}}_{\nu\nu'}(\mathbf{k})=\delta_{\nu\nu'}\varepsilon_{\mathbf{k}\nu}$.

The basic LDA+DMFT equations in the Bloch basis set are easily written, using the projection matrix elements of the local orbitals onto the Bloch functions, defined as

$$P^{\mathbf{R}}_{m\nu}(\mathbf{k}) \equiv \langle \chi^{\mathbf{R}}_{\mathbf{k}m}|\Psi_{\mathbf{k}\nu}\rangle, \quad P^{\mathbf{R}*}_{\nu m}(\mathbf{k}) \equiv \langle \Psi_{\mathbf{k}\nu}|\chi^{\mathbf{R}}_{\mathbf{k}m}\rangle. \tag{6}$$

Equations (2) and (5) then read

$$G^{\mathbf{R},\text{imp}}_{mm'}(i\omega_n) = \sum_{\mathbf{k},\nu\nu'} P^{\mathbf{R}}_{m\nu}(\mathbf{k}) G^{\text{bl}}_{\nu\nu'}(\mathbf{k},i\omega_n) P^{\mathbf{R}*}_{\nu' m'}(\mathbf{k}), \tag{7}$$

$$\Delta\Sigma^{\text{bl}}_{\nu\nu'}(\mathbf{k},i\omega_n) = \sum_{\mathbf{R}}\sum_{mm'} P^{\mathbf{R}*}_{\nu m}(\mathbf{k}) \Delta\Sigma^{\text{imp}}_{mm'}(i\omega_n) P^{\mathbf{R}}_{m'\nu'}(\mathbf{k}), \tag{8}$$

where

$$G^{\text{bl}}_{\nu\nu'}(\mathbf{k},i\omega_n) = \{[(i\omega_n + \mu - \varepsilon_{\mathbf{k}\nu})\delta_{\nu\nu'} - \mathbf{\Delta\Sigma}_{\text{bl}}(\mathbf{k},i\omega_n)]^{-1}\}_{\nu\nu'}, \tag{9}$$

$$\Delta\Sigma^{\text{imp}}_{mm'}(i\omega_n) = \Sigma^{\text{imp}}_{mm'}(i\omega_n) - \Sigma^{\text{dc}}_{mm'}. \tag{10}$$

In principle, the impurity self-energy should have a $\mathbf{R}$ index, but we have omitted it for better reading.

C. Truncating the Bloch basis set, and choice of local orbitals

As pointed out above, it is computationally impossible to implement these LDA+DMFT equations without restricting oneself to a finite subspace of N_b Bloch functions. Those Bloch functions span a certain energy window, corresponding to a subspace $\mathcal{W}$ of the total Hilbert space. Naturally, the local atomiclike orbitals $|\chi^{\mathbf{R}}_{\mathbf{k}m}\rangle$ will, in general, have a decomposition involving *all* Bloch bands. The Bloch transform of these local orbitals reads

$$|\chi^{\mathbf{R}}_{\mathbf{k}m}\rangle = \sum_{\nu} \langle \Psi_{\mathbf{k}\nu}|\chi^{\mathbf{R}}_{\mathbf{k}m}\rangle |\Psi_{\mathbf{k}\nu}\rangle. \tag{11}$$

Note that, starting from an orthonormalized set of local orbitals $\langle \chi^{\mathbf{R}}_{m\mathbf{k}}|\chi^{\mathbf{R}'}_{m'\mathbf{k}'}\rangle=\delta_{mm'}\delta_{\mathbf{R}\mathbf{R}'}\delta_{\mathbf{k}\mathbf{k}'}$, it is easily checked that the matrix $\langle \Psi_{\mathbf{k}\nu}|\chi^{\mathbf{R}}_{\mathbf{k}m}\rangle$ is unitary (from the completeness of the Bloch basis). Hence, the χ_m's can be formally viewed as Wannier functions associated with the complete basis set of all Bloch states. This property no longer holds, however, when the sum in Eq. (11) is restricted to the subset $\mathcal{W}$ of Bloch band. Defining the following:

$$|\tilde{\chi}^{\mathbf{R}}_{\mathbf{k}m}\rangle \equiv \sum_{\nu\in\mathcal{W}} \langle \Psi_{\mathbf{k}\nu}|\chi^{\mathbf{R}}_{\mathbf{k}m}\rangle |\Psi_{\mathbf{k}\nu}\rangle, \tag{12}$$

it is seen that the functions $|\tilde{\chi}^{\mathbf{R}}_{\mathbf{k}m}\rangle$ are not true Wannier functions associated with the subspace $\mathcal{W}$ since the truncated projection matrix is no longer unitary. However, these functions can be promoted to true Wannier functions $|w^{\mathbf{R}}_{\mathbf{k}m}\rangle$ by orthonormalizing this set according to

$$|w^{\mathbf{R}}_{\mathbf{k}m}\rangle = \sum_{\mathbf{R}'m'} S^{\mathbf{R}\mathbf{R}'}_{mm'}(\mathbf{k}) |\tilde{\chi}^{\mathbf{R}'}_{\mathbf{k}m'}\rangle, \tag{13}$$

where $\mathbf{S}^{\mathbf{R}\mathbf{R}'}(\mathbf{k})$ is given by the inverse square root of the overlap matrix between the Wannier-like orbitals, i.e.,

$$O^{\mathbf{R}\mathbf{R}'}_{mm'}(\mathbf{k}) \equiv \langle \tilde{\chi}^{\mathbf{R}}_{\mathbf{k}m}|\tilde{\chi}^{\mathbf{R}'}_{\mathbf{k}m'}\rangle = \sum_{\nu\in\mathcal{W}} P^{\mathbf{R}}_{m\nu}(\mathbf{k}) P^{\mathbf{R}'*}_{\nu m'}(\mathbf{k}), \tag{14}$$

$$S^{\mathbf{R}\mathbf{R}'}_{mm'}(\mathbf{k}) \equiv \{[\mathbf{O}(\mathbf{k})]^{-1/2}\}^{\mathbf{R}\mathbf{R}'}_{mm'}. \tag{15}$$

Naturally, the functions $w^{\mathbf{R}}_{m}$ are *more extended* in space than the original atomiclike functions $\chi^{\mathbf{R}}_{m}$ since they can be decomposed on a *smaller* number of Bloch functions, spanning a restricted energy range.

In the end, LDA+DMFT is implemented by taking for $\mathcal{C}$ the correlated subset generated by the set of functions $|w^{\mathbf{R}}_{\mathbf{k}m}\rangle$. Since those functions have a vanishing overlap with all Bloch functions, which do not belong to the set $\mathcal{W}$, the LDA+DMFT equations can now be put in a computationally tractable form, involving only a $N_b \times N_b$ matrix inversion within the selected space $\mathcal{W}$. Hence, the equations, which are finally implemented, read

$$G^{\mathbf{R},\text{imp}}_{mm'}(i\omega_n) = \sum_{\mathbf{k},(\nu\nu')\in\mathcal{W}} \bar{P}^{\mathbf{R}}_{m\nu}(\mathbf{k}) G^{\text{bl}}_{\nu\nu'}(\mathbf{k},i\omega_n) \bar{P}^{\mathbf{R}*}_{\nu' m'}(\mathbf{k}), \tag{16}$$

$$\Delta\Sigma^{\text{bl}}_{\nu\nu'}(\mathbf{k},i\omega_n) = \sum_{\mathbf{R}}\sum_{mm'} \bar{P}^{\mathbf{R}*}_{\nu m}(\mathbf{k}) \Delta\Sigma^{\text{imp}}_{mm'}(i\omega_n) \bar{P}^{\mathbf{R}}_{m'\nu'}(\mathbf{k}), \tag{17}$$

where

$$\bar{P}^{\mathbf{R}}_{m\nu}(\mathbf{k}) \equiv \sum_{\mathbf{R}'m'} S^{\mathbf{R}\mathbf{R}'}_{mm'}(\mathbf{k}) P^{\mathbf{R}'}_{m'\nu}(\mathbf{k}), \tag{18}$$

$$\bar{P}^{\mathbf{R}*}_{\nu m}(\mathbf{k}) \equiv \sum_{\mathbf{R}'m'} S^{\mathbf{R}\mathbf{R}'*}_{m'm}(\mathbf{k}) P^{\mathbf{R}'*}_{m'\nu'}(\mathbf{k}). \tag{19}$$

It is important to realize that the truncation to a limited set of Bloch functions was not reached by simply neglecting matrix elements between the local orbitals and Bloch functions outside this set, but rather by constructing a new set of (more extended) local orbitals such that the desired matrix elements automatically vanish, hence redefining $\mathcal{C}$ accordingly. In this view, the choices of C and of W, although independent in principle, become actually interrelated.

We also note that it is not compulsory to insist on forming true Wannier functions out of the (nonorthogonal) set $|\tilde{\chi}^{\mathbf{R}}_{\mathbf{k}m}\rangle$. It is perfectly legitimate formally to choose the correlated subspace $\mathcal{C}$ as generated by orbitals having a decomposition in $\mathcal{W}$, but not necessarily unitarily related to Bloch functions spanning $\mathcal{W}$. Although orthogonality of the χ_m's is also not compulsory, several (but not all) impurity solvers used within DMFT do require, however, that the χ_m's be orthogonal on a given atomic site. One possibility, for example, is to orthonormalize this set on identical unit cells only, i.e., requiring that $|w^{\mathbf{R}}_{\mathbf{T}m}\rangle$ and $|w^{\mathbf{R}'}_{\mathbf{T}'m'}\rangle$ in real space are orthogonal for $\mathbf{T}=\mathbf{T}'$, but not in neighboring cells $\mathbf{T}\neq\mathbf{T}'$. This amounts to orthonormalize the $|\tilde{\chi}^{\mathbf{R}}_{\mathbf{k}m}\rangle$ set with respect to the **k**-summed overlap matrix, instead of the one computed at each **k** point.

In our actual implementations, the wave functions spanning the correlated subspace $\mathcal{C}$ are obtained by following the above orthonormalization procedure, starting from atomiclike orbitals $\chi^{\mathbf{R}}_m$ centered on the atomic site **R** in the primitive unit cell. These local orbitals are either *all-electron atomic partial waves* in the PAW framework, or *pseudoatomic wave functions* when using the MBPP code. Since, in the present work, we are not dealing with full charge self-consistency including self-energy effects, the matrix elements $P^{\mathbf{R}}_{m\nu}(\mathbf{k})$ and the wave functions $|w^{\mathbf{R}}_{\mathbf{k}m}\rangle$ can be computed once and for all at the beginning of the DMFT cycle.[2] We, however, expect full-charge self-consistency effect to be the same for different choices for the local orbitals—at the condition that fixed charge calculation leads to similar results, which is the case of the present study as shown below. Details on the specific construction of the local orbitals used in this paper, and the corresponding calculation of Eq. (6) are summarized in Appendix A.

D. Physical considerations on the choice of the correlated subspace $\mathcal{C}$ and of the Wannier or Bloch space $\mathcal{W}$

Let us now discuss some physical considerations regarding the choice of the truncated Bloch space $\mathcal{W}$ when using the LDA+DMFT framework to describe a given material. Operationally, this means that a certain number of Bloch bands N_b (spanning a certain energy window) will be retained when solving Eqs. (16) and (17). As discussed above, the choice of $\mathcal{W}$ also influences the actual definition of the correlated subspace $\mathcal{C}$, since we require that the orbitals generating $\mathcal{C}$ can be expanded upon the basis functions generating $\mathcal{W}$.

Let us consider, to be specific, the case of a transition-metal oxide, such as $SrVO_3$. This material, which is described in more detail in Sec. III, has a set of three t_{2g} bands, well separated from both the O $2p$ and e_g bands, and containing nominally one d electron. We can make two rather extreme choices when describing this material with LDA+DMFT.

(i) Focus only on a very limited set of low-energy Bloch bands, such as the three t_{2g} bands, and generate $\mathcal{W}$ just from the three corresponding Bloch functions. In this case, we shall also have $\mathcal{C}=\mathcal{W}$, and the $|w^{\mathbf{R}}_{\mathbf{T}m}\rangle$ will be Wannier functions unitarily related to these three Bloch bands. Since these bands span a narrow energy window, this also means that these Wannier functions will be rather spatially extended: Although centered on vanadium atoms, they will have a sizable contribution on neighboring oxygen atoms as well. This kind of approach has been emphasized and studied in detail in Ref. 2. Of course, it is then out of the scope of such approaches to investigate the indirect effects of correlations on bands other than the t_{2g} ones.

(ii) Alternatively, one may choose a large energy window to define $\mathcal{W}$, including, in particular, all Bloch bands corresponding to O $2p$, V t_{2g}, and V e_g. Then, the orbitals $|w^{\mathbf{R}}_{\mathbf{T}m}\rangle$ defining the correlated subspace $\mathcal{C}$ may be chosen as having a component on Bloch states spanning a much larger energy range. As such, they will be more spatially localized, i.e., closer to (vanadium) atomiclike orbitals. When working with such an enlarged space $\mathcal{W}$, the physics of O $2p$ and e_g states can also be addressed.

One of the goals of the present paper is to present and compare calculations done with such different choices of $\mathcal{W}$ and $\mathcal{C}$. Of course, in a fully first-principles approach, the screened interaction matrix elements should also be calculated (e.g., in a GW framework), in a manner which is consistent with these choices of Hilbert spaces. This is left for future investigations, however, and in the present work, these matrix elements will be taken as parameters.

Let us note that the local orbitals are constructed in the present paper from an atomistic point of view. Hence, there is no "entangling problem" as the one encountered when constructing maximally localized Wannier functions for strongly hybridized band complexes. Of course, in the present formalism, the Wannier functions obtained by projection of atomic orbitals onto Bloch states belonging to a narrow energy window are not maximally localized in the sense of Ref. 11, but this feature does not bring essential differences in the results, as clear from the results reported below.

Finally, in order to relate the LDA+DMFT results to experiments performed using, e.g., photoemission spectroscopy, the real-frequency spectral functions must be obtained. This can be done using, e.g., a maximum entropy treatment of Monte Carlo data, but it is important to understand how to connect the calculated quantities to physically observable spectra. The most direct output of the LDA+DMFT calculation is the local impurity spectral function, obtained (for orbital m) as

$$A^{\text{imp}}_m(\omega) \equiv -\frac{1}{\pi}\text{Im}\, G^{\text{imp}}_{\text{mm}}(\omega + i0^+) \tag{20}$$

This also corresponds to matrix elements of the full Green's function of the solid within atomiclike orbitals χ_m's. In the LDA approximation without DMFT, it would correspond to the partial density of states for correlated orbitals. This, however, is *not* a quantity that can be easily related to photoemission experiments, since the χ_m's, when very spatially localized, extend over a large energy range. When considering a certain energy, contributions of other electrons with a different orbital character than the χ_m's will significantly contribute to the photoemission signal. Instead, if one is interested in the measured spectral function in a given energy window, one must consider the matrix elements of the full Green's function within Bloch (or Wannier) functions spanning that energy range, namely,

$$A_\nu(\omega) \equiv -\frac{1}{\pi}\text{Im}\sum_{\mathbf{k}} G^{\text{bl}}_{\nu\nu}(\mathbf{k},\omega + i0^+). \tag{21}$$

This quantity can be obtained either by first reconstructing the local self-energy on the real-frequency axis by analytical

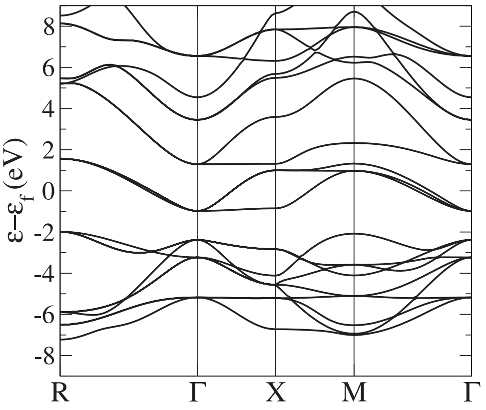

FIG. 1. LDA band structure for $SrVO_3$.

continuation of the impurity Green's function, or by direct analytic continuation of the imaginary-frequency Bloch Green's function $\mathbf{G}^{\mathrm{bl}}(\mathbf{k},i\omega_n)$. In the LDA approximation without DMFT, this quantity is by definition located in a delimited energy window and the inclusion of correlation will extend or reduce its energy range.

III. APPLICATION: $SrVO_3$

$SrVO_3$ is a $t_{2g}^1 e_g^0$ metal. It is a good test case for LDA+DMFT calculations because it is cubic and nonmagnetic and also the t_{2g} bands are isolated from both e_g and O p bands in the LDA band structure. Numerous calculations (including LDA+DMFT) and experiments have been done on this compound.[12–25] From these studies, it appears that there is a need to include correlations to correctly describe this compound. This is thus an ideal system to benchmark this implementation.

A. Local density approximation

For the PAW calculations, semicore states of V and Sr are treated in the valence. Valence states for Sr, V, and O thus include, respectively, $4s4p5s$, $3s3p4s3d$, and $2s2p$ states. PAW matching radii are 1.52, 1.92, and 2.35 a.u., respectively. The experimental cubic crystal structure is used (space group $Pm\bar{3}m$ with lattice constant of 7.2605 a.u.). Atomic data are generated using ATOMPAW.[26,27] Calculations are done with the PAW code ABINIT.[28,29] The density of states and the LDA band structure are shown in Figs. 1 and 2. The projection of the density of states on O p, V t_{2g}, and V e_g and the character of the bands (see Fig. 3) show that bands with O p and with V t_{2g} characters are indeed isolated from the others. The hybridization between oxygen and vanadium orbitals is nevertheless clearly seen.

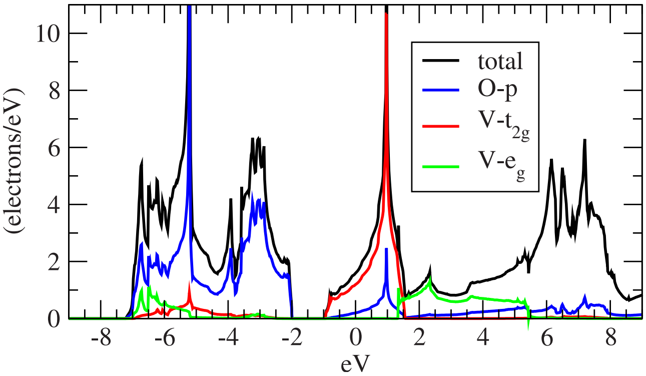

FIG. 2. (Color online) LDA total and projected density of states for $SrVO_3$.

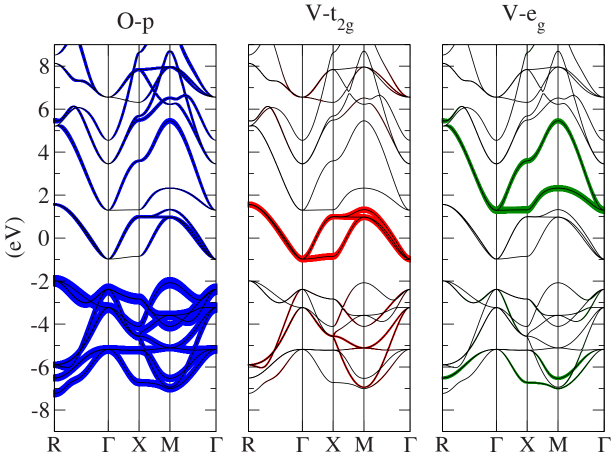

FIG. 3. (Color online) LDA band structure for $SrVO_3$ computed in PAW, with "fatbands" to show the amplitude of the projection of each band on a given atomic orbital (O p, V t_{2g}, and V e_g).

B. LDA+DMFT

In this section, we will present the results of our scheme based on the projection of local orbitals upon Bloch states [projected local orbitals (PLO)]. As previously emphasized, the number of KS bands used for the projection has to be chosen in a given range of energy. The extension of the Wannier-like renormalized orbitals [Eq. (13)] will depend on this choice. We will use the fact that the band structure of $SrVO_3$ is made of isolated blocks. The choices of $\mathcal{W}$ are summarized in Table I. We will compare the results with LDA+DMFT calculations done[2] with MLWFs (see Appendix C).

Calculations have been carried out at $T=0.1$ eV. A density-density interaction vertex is used,[30] with J

TABLE I. Different choices for the number of KS states N_b used within the PLO scheme of LDA+DMFT. The energy range spanned by these bands is also indicated. $N_b=3$ corresponds to only the three bands of mainly t_{2g} character. $N_b=12$ corresponds to the nine O p bands and the three V t_{2g} bands (see Fig. 3). $N_b=21$ corresponds to a large number of bands, including e_g bands and seven bands above. N_{imp} is the number of orbitals in the impurity model. When used, MLWF will be extracted with the same parameters.

N_b	N_{imp}	Energy range (eV)
3	3	$-1.5 \rightarrow 1.8$
12	3	$-8.0 \rightarrow 1.8$
21	5	$-8.0 \rightarrow 13.0$

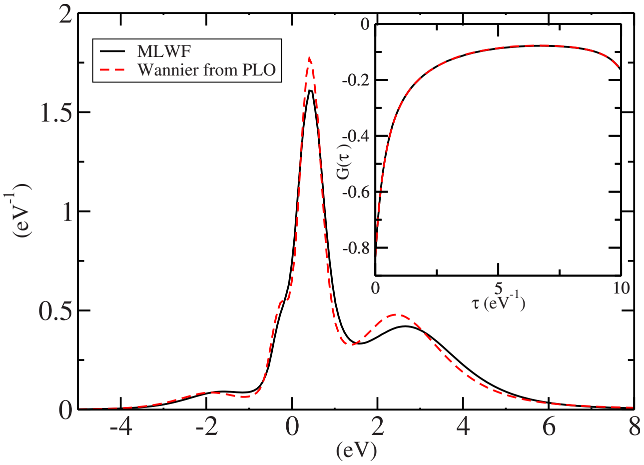

FIG. 4. (Color online) Local impurity spectral function of $SrVO_3$ for $U=4$ eV within LDA+DMFT using the MLWF basis and the PLO scheme ($N_b=3$). Inset: Green's function in imaginary time. Note that when using such a small (t_{2g}) energy window, the impurity spectral function and Bloch-resolved spectral function coincide.

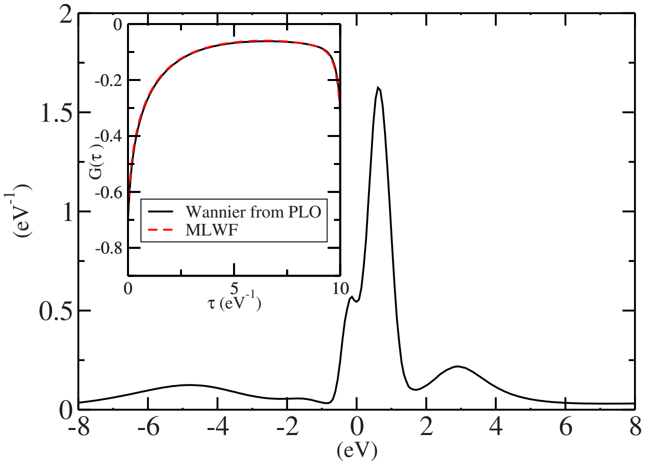

FIG. 5. (Color online) Local impurity spectral function of $SrVO_3$ for $U=6$ eV within LDA+DMFT using the PLO scheme ($N_b=12$). Inset: Green's function in imaginary time for both the PLO and MLWF schemes.

$=0.65$ eV, which is similar to another study.[2] The Hubbard parameters $U=4$ eV and $U=6$ eV have been used in the calculations. The impurity problem of DMFT is solved with Hirsch–Fye quantum Monte Carlo with 128 time slices. The around mean-field (AMF) formulation of the double counting is used in these calculations (see Appendix B).

1. t_{2g} bands in the basis for $\mathcal{W}$ ($N_b=3$)

Spectral functions obtained from the PLO and MLWF schemes are reproduced in Fig. 4.

The impurity Green's functions obtained within the two schemes are in very good agreement: They both show a lower Hubbard band at -1.8 eV and an upper Hubbard band at 2.5 eV. This shows that the two schemes contain the same physical content and that PLOs constructed from a small energy window give very similar results to *maximally localized* Wannier functions.[2]

2. O *p* and V t_{2g} bands in the basis for $\mathcal{W}$ ($N_b=12$)

O *p* states are now included in the calculation. MLWFs of t_{2g} symmetry will thus be more localized, and will have less O *p* character, because the MLWFs of O *p* symmetry will have mainly the weight on oxygen atoms. In the PLO scheme also, the Wannier orbitals will include more Bloch states, and thus will be closer to localized local orbitals χ_m. In other words, because the Wannier function of the local impurity problem is now constructed from a wider energy window, which includes O *p* states, the corresponding spectral function will have a non-negligible weight in the energy area of the O *p* states. In the LDA case without Hubbard correction, this spectral function would, in fact, be identical to the projected t_{2g} density of states plotted in Fig. 2.

In order to first benchmark our calculation using PLO with respect to calculations using MLWF, we plot in Fig. 5 the comparison of the impurity Green's function in the two cases. The local impurity spectral function shows a large hybridization band in the area of the O *p* states. We emphasize that this band is mainly not a many-body feature: It is a manifestation of hybridization with oxygen states, and is readily visible at the pure LDA level. The lower Hubbard band is, in fact, partly contained in this spectral function as a shoulder in the hybridization band around -1.5 eV. However, disentangling the Hubbard band from the hybridization contribution is somewhat difficult to achieve with the maximum entropy method. The upper Hubbard band is visible in the impurity spectral function, as a hump around 3.0 eV.

These many-body features (lower and upper Hubbard bands) are more clearly revealed, however, by looking at the (**k**-averaged) spectral function of t_{2g} Bloch states (21). It is also useful to look at the spectral functions of the other Bloch states in the basis set. The summation of these spectral functions over bands belonging to the same group (e.g., O *p* or V t_{2g} states, i.e., bands with mostly O *p* or V t_{2g} character) enables us to have a clear view on the impact of correlation on LDA bands. The spectral functions of O *p* states and V t_{2g} states are plotted in Fig. 6. We emphasize that these spectral functions do not correspond to atomiclike orbitals with O *p* character and V t_{2g} character (the latter being the impurity spectral function plotted in Fig. 5).

The Hubbard band appears as a hump in the **k**-averaged Bloch spectral function corresponding to the t_{2g} states for $U=4$ eV. This hump is located between the O *p* states and the t_{2g} state quasiparticle peak. The Hubbard band is more clearly resolved for $U=6$ eV. In this case, however, it is hidden inside the O *p* band. We shall come back to this point at the end of this section.

The fact that a higher value of U is necessary in this case (with respect to $N_b=3$) to recover the lower Hubbard band is consistent with the fact that Wannier functions are more localized for $N_b=12$.

3. Large number of bands in the basis for $\mathcal{W}$ ($N_b=21$)

In this case, the e_g states are included in the calculation. The impurity model is now solved with all five *d* orbitals.

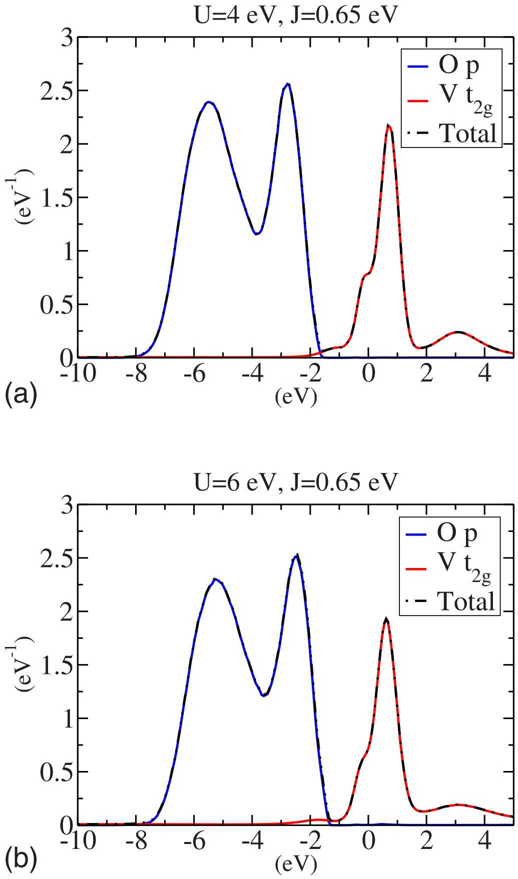

FIG. 6. (Color online) Total Bloch spectral function for $\mathrm{SrVO_3}$, and spectral functions of O p and V t_{2g} states for $U=4$ eV (a) and $U=6$ eV (b) within LDA+DMFT using the PLO scheme ($N_b=12$). These spectral functions are not the local orbital projected spectral functions (see text): The t_{2g} local impurity spectral functions are plotted in Fig. 5.

The agreement between impurity Green's functions computed in the MLWF and PLO schemes is shown in Fig. 7. Note again that resolving the Hubbard band from the impurity Green's function is difficult because this quantity is dominated by hybridization effects with oxygen states. Again, we have to turn to Bloch-resolved spectral functions, plotted in Fig. 8 for O p, V t_{2g}, and V e_g Bloch states. The results are quite similar to the previous ones with $N_b=12$, with a lower Hubbard band clearly visible for the t_{2g} states at about -2.0 eV in the spectral function. Note that here we use $U=6$ eV. It shows that the basis of Kohn–Sham bands is adapted to the calculation: The convergence of physical properties as a function of the number of bands is rather fast.

4. Discussion

The comparisons made above should not be simply thought of as a convergence study as a function of the size of the Bloch basis $\mathcal{W}$. Indeed, as N_b is increased, we change the spatial extension of the local orbitals [Eq. (13)] spanning the correlated subspace, so that the DMFT treatment does not apply to the same objects. Convergence studies with fixed χ_m's could also be performed, but this is not the main scope of this paper.

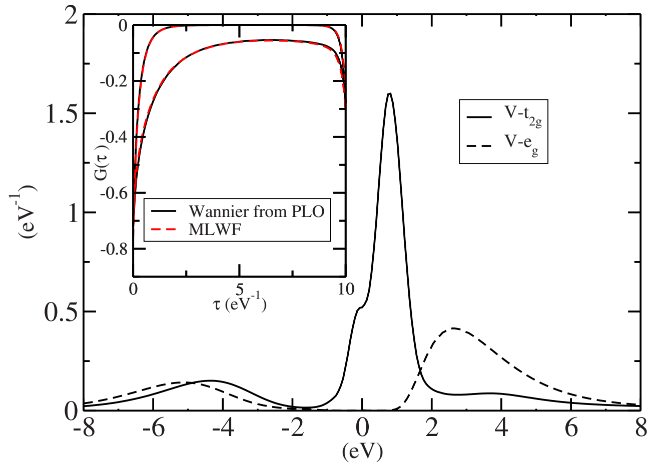

FIG. 7. (Color online) Local impurity spectral function of $\mathrm{SrVO_3}$ for $U=6$ eV within LDA+DMFT using the PLO scheme ($N_b=21$). Inset: Green's function in imaginary time for both the PLO and MLWF schemes.

Instead, we would like to emphasize some of the physical issues when applying DMFT to different local orbitals with different degrees of spatial localization. As we have seen, for more localized orbitals (larger N_b), we have to increase the value of the on-site U on the vanadium site to get consistent results. This is of course physically expected. We see, however, that the main features of the spectral function (see Fig. 9) are almost identical for $N_b=12$ and $N_b=21$ with similar values of U. The lower Hubbard band (between -1.7 and -2.0 eV) is not far from the position experimentally found[17,21,22,25,31] (between -1.5 and -2.0 eV). The Hubbard band (between 2.5 and 3 eV) is also in the range of experiments (2.5 eV).

In the results that we have obtained, the lower Hubbard band is rather systematically at an energy in which oxygen states already give a sizable contribution in the total density of states. Experiments, however, seem to suggest a somewhat larger separation. We believe that this is due to the fact that

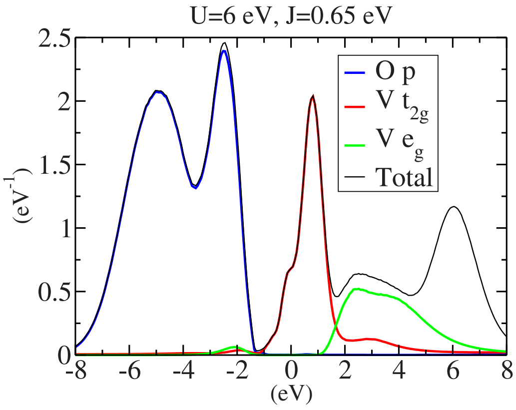

FIG. 8. (Color online) Total Bloch spectral function for $\mathrm{SrVO_3}$, and spectral functions of O p, V t_{2g}, and V e_g states for $U=6$ eV within LDA+DMFT using the PLO scheme ($N_b=21$). These spectral functions are not the local orbital projected spectral functions (see text): The t_{2g} and e_g local impurity spectral functions are plotted in Fig. 7.

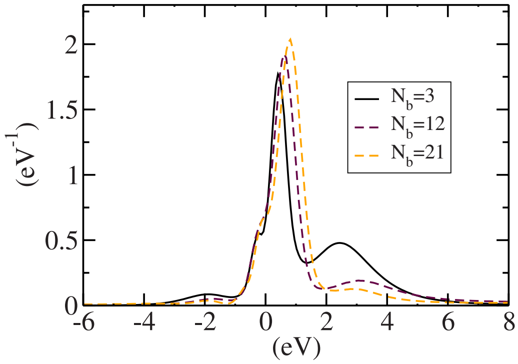

FIG. 9. (Color online) Spectral function of t_{2g} Bloch states for $SrVO_3$ within the PLO scheme of LDA+DMFT. For $N_b=12$ and $N_b=21$, $U=6$ eV. For $N_b=3$, $U=4$ eV.

the relative location of O and V t_{2g} states is not accurately obtained at the LDA level, and that a better starting point (such as GW) is required to handle this problem with better accuracy. Indeed, we have verified that the intensity of the lower Hubbard band and especially of the upper Hubbard band (as revealed in the Bloch-resolved t_{2g} spectral function) is very sensitive to the precise value of the double-counting correction that is used. This is shown in Fig. 10, in which we have slightly shifted downward the O 2p states with respect to the V t_{2g} ones by purposely choosing a smaller value of the double-counting correction (3.6 eV instead of 6.6 eV). The more isolated the t_{2g} states are, the more prominent are the correlation effects within that band (for a given U).

In future work, calculations with extended basis sets should naturally face the issue of calculating the on-site Coulomb interaction from first principles, but also of taking into account Coulomb repulsion terms U_{pp} on the oxygen sites, as well as intersite repulsions U_{pd} between vanadium and oxygen. We note that treating the latter in the Hartree approximation precisely brings in a correction to the relative position of oxygen and vanadium states, of the same nature than the double-counting terms.

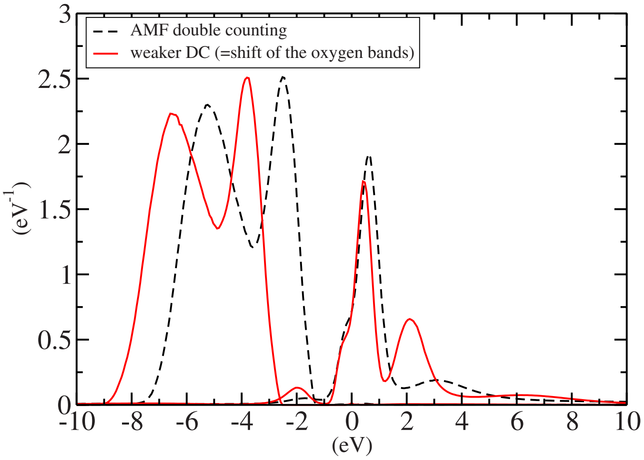

FIG. 10. (Color online) Spectral functions of O p and V t_{2g} *states* for $U=6$ eV within LDA+DMFT using the PLO scheme ($N_b=12$). Two values of the double-counting shift are used: 6.6 (AMF) and 3.6 eV.

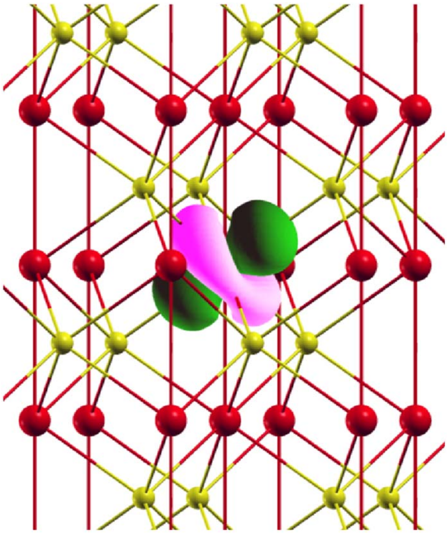

FIG. 11. (Color online) Projected $\beta-$NiS structure with a local Ni(e_g) orbital obtained from a MLWF construction using the block of 16 Ni(3d)/S(3p) bands. The c axis is identical to the vertical axis.

The general conclusion of this study of $SrVO_3$ at this stage is that our formalism is able to describe the main features of the experimental function within a general formalism, which can take into account all states in the basis.

IV. APPLICATION: β-NiS

The hexagonal form of nickel sulfide (β-NiS) has attracted a lot of interest over the years since it exhibits a first-order electronic phase transition[32] at about 260 K. Whereas the high-temperature phase may be classified as a paramagnetic metal, below the transition β-NiS shows antiferromagnetic order and the resistivity behavior corresponds to characteristics of a semimetal[33] or a degenerate semiconductor.[34] Hence, the term "antiferromagnetic nonmetal" is commonly used for the low-temperature phase. Note that hexagonal NiS is only metastable at room temperature; the true stable phase is given by the millerite structure.[35] The crystal structure (Fig. 11) of β-NiS is of the NiAs type (space group $P6_3/mmc$) with two unit cells in the primitive cell.[36] In this rather simple structure, the NiS_6 octahedra share edges within the ab plane and share faces along the c axis. There is a slight decrease of the cell parameters ($\delta a/a \sim 0.3\%$, $\delta c/c \sim 1\%$) below the transition, which gives rise to a volume collapse of the order of 2%. Our aim in this work is not to perform a detailed study of the metal-to-nonmetal transition of β-NiS, since this would involve deeper considerations concerning the role of magnetism above and below the transition. For an overview of this still controversially discussed topic, see, e.g., the review by Imada *et al.*[12]

Here, we mainly want to use the high-temperature phase of β-NiS as an example for a correlated metal with strongly hybridized Ni(3d) and S(3p) states, formally in the charge-transfer regime of the Zaanen–Sawatzky–Allen classification scheme.[37] In this regard, it will become clear that this com-

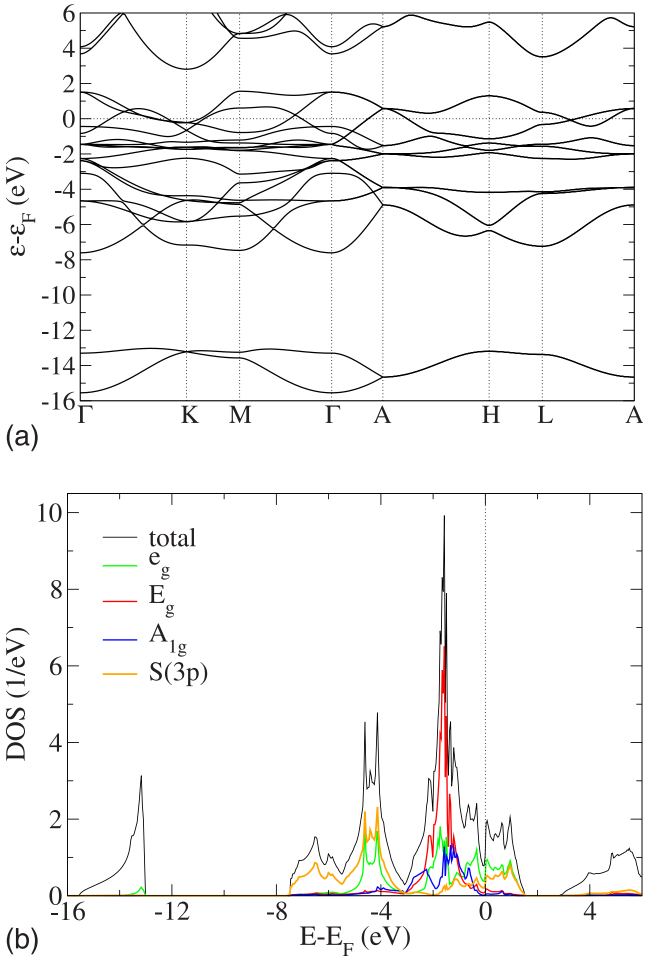

FIG. 12. (Color online) LDA data for β-NiS. (a) Band structure. (b) DOS. For the local Ni($3d$)/S($3p$)-DOS, the cutoff radius was one-half the nearest-neighbor distance.

pound may not easily be treated in the “traditional” LDA +DMFT scheme via projecting solely onto low-energy states close to the Fermi level. Thus, the goal is to use the here outlined projection technique of interfacing LDA with DMFT in order to explore the importance of electronic correlations for the local spectral function.

A. Local density approximation investigation

Electronic structure calculations for β-NiS date back to the original work of Mattheiss.[38] Here, the DFT-LDA calculations are performed with a mixed-basis pseudopotential (MBPP) code[39] described in Appendix A 2. For the lattice parameters, we use a=3.440 Å and c=5.351 Å from Ref. 36. Figure 12 shows the resulting band structure and density of states (DOS) from this computation. It is seen that the common block of hybridized Ni($3d$) and S($3p$) bands is isolated from the remaining bands. The dominantly S($3s$)-like bands are ~5.5 eV below in energy,[40] while the bands above starting with mainly Ni($4s$) character are separated by ~1.2 eV from that block. The latter has a width of ~9 eV and consists of three prominent peaks below the Fermi level. The dominant $d^8\mathbf{L}$ peak[40] at -1.5 eV (P_1), a second at -4.4 eV (P_2), and the last at -6.5 eV (P_3). Whereas P_2 has mixed Ni($3d$)/S($3p$) character, P_3 is a nearly pure S($3p$) peak and does not stem from bonding between Ni and S.

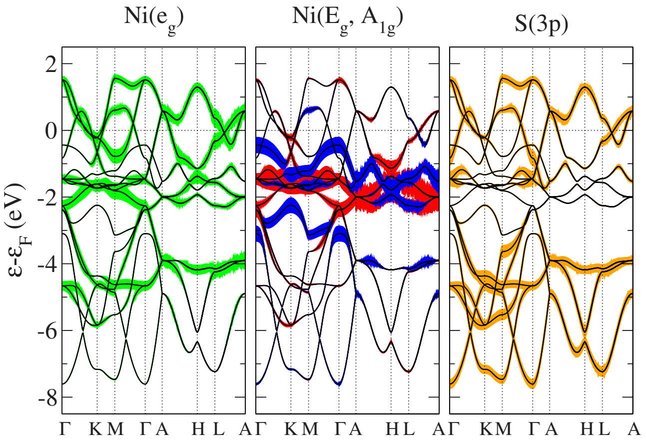

FIG. 13. (Color online) LDA fatband decomposition for β-NiS. (red/gray) Ni(E_g) and (blue/dark) Ni(A_{1g}). The local Ni($3d$)/S($3p$) projection cutoff radius was one-half the nearest-neighbor distance.

In order to obtain more detailed information about the involvement of the different orbital sectors, the orbital-resolved DOS is additionally incorporated in Fig. 12(b). Furthermore, the fatband representation of the decomposition of the Bloch bands is presented in Fig. 13. Because of the hexagonal symmetry, the Ni($3d$) multiplet splits into two degenerate e_g levels, two degenerate E_g levels, and one A_{1g} level per atom, respectively. As usual, the e_g states hybridize more strongly with the S($3p$) states than the remaining (E_g,A_{1g}) states. Due to the increasingly filled d shell of Ni, the (E_g,A_{1g}) levels are moreover also nearly completely occupied in β-NiS. In numbers, the LDA filling, including degeneracy, amounts to (2.9;3.9,1.9) for (e_g;E_g,A_{1g}). The fatband representation clearly shows that the hybridization between the different orbitals is strong and it is not quite obvious to single out a low-energy regime for this compound within the central block of bands. Although the bands at the Fermi level appear to be dominantly of e_g character, the corresponding orbitals have a strong weight at lower energy, too. Despite the strong filling of the (E_g,A_{1g}) states, abandoning those orbitals in a minimal Hamiltonian description of β-NiS is likely to fail. Fluctuations originating from holelike states may be important in the end to reach a better understanding of the complex magnetic behavior of this material. Note also in this respect that the effective bandwidth of the energy range where the e_g character is manifest is roughly twice as large as the corresponding energy range for (E_g,A_{1g}). Hence, this reduced relative bandwidth for (E_g,A_{1g}) within the Ni($3d$) multiplet will also have influence on the degree of the orbital-resolved correlation effects.

B. LDA+DMFT investigation

The influence of correlation effects in β-NiS has been experimentally and theoretically investigated by several authors.[40–45] It is generally believed that this compound is moderately correlated in view of the strong hybridization of

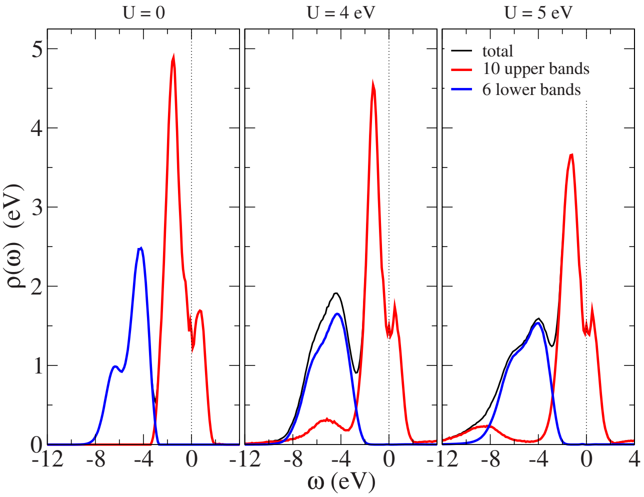

FIG. 14. (Color online) The LDA+DMFT local spectral function for β-NiS derived from the local Green's function in Bloch basis at $\beta=10\ \text{eV}^{-1}$. The contribution from the upper ten bands of the Ni(3d)/S(3p) block was encoded red, and the one from the lower six bands was encoded blue. This guidance to the eyes should roughly separate dominant Ni(3d) from dominant S(3p) character.

the ~3/4 filled e_g states with sulfur. A value for the Hubbard U of the order of 4–5 eV was estimated from modeling the measured spectral function derived from photoemission experiments.[41,43,45] These experiments in the metallic phase are in rough agreement with the shown LDA DOS below the Fermi level insofar as they also reveal three peaks with comparable relative intensity as the theoretical set (P_1, P_2, P_3). However, an effective single-particle picture appears to be insufficient to understand those peaks, especially when going to the nonmetallic phase.[43] It is theoretically expected that a lower Hubbard band, i.e., satellite, originating from the Ni(3d) states should be located within the Bloch states deep in energy (starting around 6 eV) and dominantly characterized by S(3p). This idea relies on the fact that β-NiS may be viewed as belonging to the charge-transfer category of transition-metal chalcogenides, yet not being that strongly correlated for the lower Hubbard band to appear below the S(3p) states.

The strong hybridization between Ni(3d) and S(3p) renders the PLO version of the LDA+DMFT method most suitable for this compound. Concerning the value of U, we chose a pragmatic approach and performed the calculations for two possibly reasonable choices, i.e., $U=4$ eV and $U=5$ eV. The value of J is certainly less materials dependent and was fixed to $J=0.7$ eV. In order to take care of the double counting, we used the formalism of fixing the local total charge (see Appendix B). Note that for the present crystal structure, there are two symmetry-equivalent Ni atoms in the primitive unit cell, i.e., two correlated sites $\mathbf{R}$. The local Green's function and self-energy were thus computed by symmetrizing the site-resolved quantities. For the projection onto local orbitals, we limited the number of bands to $N_b=16$, i.e., all bands of the central block around the Fermi level are used. This renders the corresponding correlated subspace already rather localized, e.g., the effective Ni(3d)-like WFs from this set of bands are not expected to leak much to the sulfur sites (see also Fig. 11).

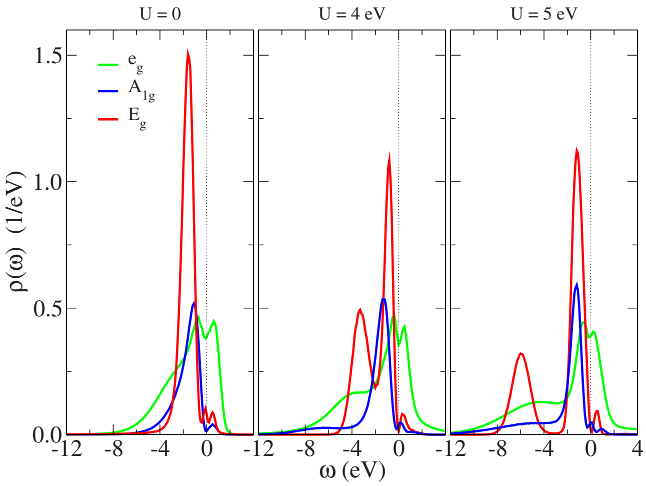

FIG. 15. (Color online) The corresponding LDA+DMFT local impurity spectral function for β-NiS at $\beta=10\ \text{eV}^{-1}$.

By explicitly including the correlation effects, the orbital-resolved fillings in the 3d shell of Ni do not relevantly change; thus, effects due to changes in orbital populations induced by correlations are not expected to play an important role for this compound. Figure 14 exhibits the resulting local spectral function for the different values of U at inverse temperature $\beta=10\ \text{eV}^{-1}$. It is seen that the influence of correlation effects on the metallic spectral function is indeed rather subtle for this compound. A lower Hubbard band appears to show up for U as large as 4 eV within the dominant S(3p) energy regime. It is, however, hard to extract this atomiclike excitation from the total spectral function (as in experiment).[40,45] The plot of the *impurity* spectral function in Fig. 15 reveals that the (E_g,A_{1g}) orbitals yield indeed effective bands with smaller bandwidth than the e_g orbitals. It seems that especially the E_g orbitals are significantly susceptible to the strong-correlation effects, since showing the most pronounced atomiclike excitation within the set of d bands in this illustration. Note, however, the difference between Figs. 14 and 15. The spectral function in Fig. 15 resembles the correlation effects for the somewhat artificial "naked" d orbitals [somehow corresponding to the projections in Fig. 12(b)], without the contribution from strongly hybridized S(3p) orbitals. Hence, Fig. 14 reveals the "true" spectral function stemming from the fully hybridized bands.

In the end, the total spectral function computed for $U=5$ eV shows close resemblance to recent experimental curves obtained from photoemission.[45] Note, however, that it still appears tricky to disentangle the lower Hubbard band from the P_3 peak of in principle pure S(3p) content. Our calculation suggests that the correlation effects also have an impact on the lowest S(3p)-like states. Further studies are necessary to clarify this issue.

V. CONCLUSIONS

We have implemented an effective and flexible LDA+DMFT scheme into two electronic structure formalisms based on a plane-wave description, i.e., projector augmented wave and mixed-basis pseudopotential. The orbitals defining the correlated subspace $\mathcal{C}$, in which many-body effects are included, are constructed by projecting local atomiclike orbitals onto a restricted set $\mathcal{W}$ of Kohn–Sham Bloch states, similar to the procedure adopted in Ref. 1. Orthonormalization of the projected orbitals yields effective Wannier functions spanning $\mathcal{C}$. These WFs are not unique: They depend on the energy window covered by the Bloch functions in $\mathcal{W}$ (the larger the window, the more localized the WFs are). Although more sophisticated constructions[8,11] of explicit WFs will surely remain an important tool in the LDA+DMFT context, we feel that the more straightforward projection technique will render future developments in this area easier and more efficient.

Using this method, we have investigated $SrVO_3$ and compared different implementations involving different choices for the set of Bloch states $\mathcal{W}$ and for the corresponding local orbitals spanning $\mathcal{C}$. We have shown that the basic physical findings for this compound are consistent with previous LDA+DMFT treatments, independently of the chosen implementation. However, the present study allows for an explicit treatment of ligand states, which raises several issues that should be the subject of further studies. One of these issues is a first-principles determination of the on-site Coulomb matrix elements in the different choices of local orbitals and basis set. Our study supports the expected fact that a larger value of U_{dd} has to be taken when a larger energy range (and more localized orbitals) is considered. Furthermore, a proper treatment of the on-site repulsion on oxygen sites U_{pp}, as well as of oxygen–transition-metal intersite repulsion U_{pd} should certainly be considered. This issue is tightly connected to the choice of double-counting correction, which, as we have shown, plays a significant role.

We have also presented a LDA+DMFT study of metallic β-NiS, a charge-transfer compound for which the inclusion of ligand states is crucial. More detailed studies, extending also into the nonmetallic regime, are needed in order to gain more insight into this "traditional companion" of the more famous NiO compound where such investigations recently took place.[46,47]

In general, the explicit inclusion of the ligand states in the LDA+DMFT description, based on generic highly accurate electronic structure codes, will open the door to new possibilities for the investigation of strong-correlation effects in real materials.

Note added. Recently, we became aware of the related work of Korotin *et al.*,[56] who also reported on an implementation of LDA+DMFT in a pseudopotential plane-wave framework.

ACKNOWLEDGMENTS

We are grateful to O. K. Andersen, F. Aryasetiawan, S. Biermann, T. Miyake, A. Poteryaev, L. Pourovskii, J. Tomczak, and M. Torrent for collaborations and discussions related to the subject of this paper. We acknowledge support from CNRS, Ecole Polytechnique, the Agence Nationale de la Recherche (under contract *ETSF*), and the Deutsche Forschungsgemeinschaft (DFG) within the scope of the SFB 668.

APPENDIX A: CALCULATION OF THE PROJECTION $P^{\mathbf{R}}_{m\nu}$

In this appendix, we describe the details of the calculation of the projection $P^{\mathbf{R}}_{m\nu}$ from KS Bloch states onto local orbitals in both the PAW[48] and the MBPP[49] method.

1. Projector augmented-wave method

In the projector augmented-wave formalism, two kinds of atomic functions are used: the pseudo-wave-function $\tilde{\varphi}$ and the true wave function φ. They are used to recover the correct nodal structure of the wave function near the nucleus [see Eq. (9) of Blöchl[48]]. A direct calculation of the projection $P^{\mathbf{R}}_{m\nu}(\mathbf{k})$ would thus require to compute the three terms resulting from this equation, namely ($\tilde{p}_i$ is the projector n_i for angular momenta l_i, and its projection m_i),

$$P^{\mathbf{R}}_{m\nu}(\mathbf{k}) = \langle \chi^{\mathbf{R}}_m | \tilde{\Psi}_{\mathbf{k}\nu}\rangle + \sum_i \langle \tilde{p}_i | \tilde{\Psi}_{\mathbf{k}\nu}\rangle (\langle \chi_m | \varphi_i\rangle - \langle \chi^{\mathbf{R}}_m | \tilde{\varphi}_i\rangle). \tag{A1}$$

However, atomic d or f wave functions are mainly localized inside spheres. As a result, we can compute the projection only inside sphere, in the spirit of current LDA+U implementation[50,51] in PAW. In this particular case, the first and third terms of Eq. (A1) cancel each other. This cancellation is only exact for a complete set of projectors in the energy range of the calculation. This completeness can be easily tested during the construction of projectors and partial waves. The projection thus writes as a sum over projectors $\tilde{p}_{n_i}$ as follows:

$$P^{\mathbf{R}}_{m\nu}(\mathbf{k}) = \sum_{n_i} \langle \tilde{p}_{n_i} | \tilde{\Psi}_{\mathbf{k}\nu}\rangle \langle \chi^{\mathbf{R}}_m | \varphi_{n_i}\rangle. \tag{A2}$$

We note that integrals in this equation are computed only inside sphere. It implies that the projection is done on an unnormalized wave function χ. Nevertheless, the latter normalization of the projection $P^{\mathbf{R}}_{m\nu}(\mathbf{k})$ will make a normalization of χ redundant. This implementation has been made with the code ABINIT.[28,29]

Additionally, we implemented the proposed LDA+DMFT scheme in a somehow simplified interfacing with the PAW-based Vienna *ab initio* simulation package[52] (VASP) by using *only* the PAW projectors from the standard output for $P^{\mathbf{R}}_{m\nu}(\mathbf{k})$. Although approximate, this latter identification yielded (after, of course, proper normalization) very similar results in comparison with the more well-defined explicit coding described above.

2. Mixed-basis pseudopotential method

The combination of norm-conserving pseudopotentials with a mixed basis of plane waves and localized orbitals in order to represent the pseudocrystal wave function is the main ingredient[49] of our employed mixed-basis pseudopotential code.[39] More concretely, the MBPP band-structure code uses the following representation for the KS pseudo-wave-functions:

$$|\Psi_{\mathbf{k}\nu}\rangle = \sum_{\mathbf{G}} \psi^{\mathbf{G}}_{\mathbf{k}\nu}|\mathbf{k}+\mathbf{G}\rangle + \sum_{\gamma lm} \beta^{\gamma l}_{\mathbf{k}\nu m}|\phi^{\gamma l}_{\mathbf{k}m}\rangle, \qquad (A3)$$

with

$$\langle \mathbf{r}|\mathbf{k}+\mathbf{G}\rangle = \frac{1}{\sqrt{\Omega_c}} e^{i(\mathbf{k}+\mathbf{G})\cdot\mathbf{r}}, \qquad (A4)$$

$$\langle \mathbf{r}|\phi^{\gamma l}_{\mathbf{k}m}\rangle = \sum_{\mathbf{T}} e^{i\mathbf{k}\cdot(\mathbf{T}+\mathbf{R}_\gamma)}\phi^{\gamma l}_{m}(\mathbf{r}-\mathbf{T}-\mathbf{R}_\gamma). \qquad (A5)$$

In these equations, γ denotes the atom in the unit cell, Ω_c is the volume of the unit cell, ν is the band, and l,m are the angular momentum and azimuthal quantum number. The plane waves in this basis extend up to a chosen energy cutoff E^{pw}. The analytical form of the local orbitals $\phi^{\gamma l}_m$ reads

$$\phi^{\gamma l}_m(\mathbf{r}') = i^l f_{\gamma l} K_{lm}(\hat{\mathbf{r}}'), \quad \mathbf{r}' = \mathbf{r}-\mathbf{T}-\mathbf{R}_\gamma, \qquad (A6)$$

whereby K_{lm} describes a cubic harmonic and the radial function $f_{\gamma l}$ is an atomic pseudo-wave-function modified with a proper decay and cutoff function in order for $f_{\gamma l}$ to vanish beyond some chosen radial cutoff $r_c^{(\gamma l)}$. Note that the local orbitals are orthonormal and by definition do not overlap between neighboring sites, i.e.,

$$\int_0^{r_c^{(\gamma l)}} dr |f_{\gamma l}(r)|^2 r^2 = 1, \qquad (A7)$$

$$\langle \phi^{\gamma' l'}_{m'}|\phi^{\gamma l}_m\rangle = \delta_{\gamma'\gamma}\delta_{l'l}\delta_{m'm}. \qquad (A8)$$

By identifying the local orbitals $\phi^{\gamma l}_m$ as the objects to project onto (i.e., the χ_m in the outlined LDA+DMFT formalism), the projection $P^{\mathbf{R}}_{m\nu}(\mathbf{k})$ may be written with the help of Eqs. (A3) and (A8) as

$$P^{\mathbf{R}}_{m\nu}\gamma(\mathbf{k}) = \langle \phi^{\gamma l}_{\mathbf{k}m}|\Psi_{\mathbf{k}\nu}\rangle = \sum_{\mathbf{G}} \psi^{\mathbf{G}}_{\mathbf{k}\nu}\langle \phi^{\gamma l}_{\mathbf{k}m}|\mathbf{k}+\mathbf{G}\rangle + \beta^{\gamma l}_{\mathbf{k}\nu m}. \qquad (A9)$$

APPENDIX B: DOUBLE COUNTING

The double-counting shift [used in Eq. (5)] is necessary in the formalism in order to correct the fact that electronic correlations are already treated in an average way within LDA. Since there is no unique way to extract this double counting from LDA, two alternative formulations were used in this work. First, the so-called around mean-field[42,53] (AMF) method, which is usually adequate for metals. Second, a different formalism in which the double counting is such that the electronic charge computed from the local noninteracting Green's function and the one computed from the interacting impurity Green's function is constrained to be identical:

$$\mathrm{Tr}\, G_{\mathrm{imp}}(i\omega_n) = \mathrm{Tr}\, G^{(0)}_{\mathrm{imp}}(i\omega_n). \qquad (B1)$$

Here, $G^{(0)}_{\mathrm{imp}}$ is generally given by

$$G^{\mathbf{R},\mathrm{imp},(0)}_{mm'}(i\omega_n) = \sum_{\mathbf{k}}\sum_{\alpha\alpha'} \langle \chi^{\mathbf{R}}_{\mathbf{k}m}|B_{\mathbf{k}\alpha}\rangle\langle B_{\mathbf{k}\alpha'}|\chi^{\mathbf{R}}_{\mathbf{k}m'}\rangle\{[i\omega_n+\mu - \mathbf{H}_{\mathrm{KS}}(\mathbf{k})]^{-1}\}_{\alpha\alpha'}. \qquad (B2)$$

Alternatively, one may want to use the Weiss field $\mathcal{G}(i\omega_n)$ instead of the local noninteracting Green's function in Eq. (B1). Note that in any case this formalism asks for an additional convergence parameter $\delta\mu_{dc}$ to fulfill Eq. (B1). Hence, this parameter has to be iteratively found together with the total chemical potential μ in the DMFT cycle.

For $\mathrm{SrVO_3}$ (with $N_b=12$), the respective double-counting shifts are 6.6 (AMF) and 5.5 eV (fixing local charge). However, these two calculations give very similar results.

APPENDIX C: MAXIMALLY LOCALIZED WANNIER FUNCTIONS IN PROJECTOR AUGMENTED WAVE

To define maximally localized[11] WFs, we need the following quantity:

$$M^{(\mathbf{k},\mathbf{b})}_{m,n} = \langle \Psi_{n,\mathbf{k}}|e^{-i\mathbf{b}\cdot\mathbf{r}}|\Psi_{m,\mathbf{k}+\mathbf{b}}\rangle. \qquad (C1)$$

In the PAW framework, this quantity can be expressed as a function of the pseudo-wave-function $\tilde{\Psi}$, the projectors p, the atomic wave function ϕ, and the pseudoatomic wave function $\tilde{\phi}$. We use the expression for an operator A within the PAW formalism [Eq. (11) of Blöchl[48]]. We thus obtain

$$M^{(\mathbf{k},\mathbf{b})}_{m,n} = \langle \tilde{\Psi}_{\mathbf{k},m}|e^{-i\mathbf{b}\cdot\mathbf{r}}|\tilde{\Psi}_{\mathbf{k}+\mathbf{b},n}\rangle + \sum_{i,j}\langle \tilde{\Psi}_{\mathbf{k},m}|\tilde{p}_i\rangle\langle \tilde{p}_j|\tilde{\Psi}_{\mathbf{k}+\mathbf{b},n}\rangle \times (\langle \phi_i|e^{-i\mathbf{b}\cdot\mathbf{r}}|\phi_j\rangle - \langle \tilde{\phi}_i|e^{-i\mathbf{b}\cdot\mathbf{r}}|\tilde{\phi}_j\rangle). \qquad (C2)$$

A similar expression has been used for ultrasoft pseudopotentials by Ferretti *et al.*[54] The first term is computed in the Fourier basis, whereas the second is computed in the radial grid. We use the expansion of $e^{-i\mathbf{b}\cdot\mathbf{r}}$ in spherical harmonics and Bessel functions in order to compute its expectation value over atomic wave functions.

The overlap matrix $M^{(\mathbf{k},\mathbf{b})}_{m,n}$ is used to minimize the spread and localize the WFs. This is done with the publicly available WANNIER90 code.[55]

Our calculation of the overlap is tested on t_{2g} MLWF for $\mathrm{SrVO_3}$ using only the three KS t_{2g} bands. The spread of one of the WFs for an $8\times8\times8$ k-point grid centered on the Γ point with our implementation is 6.96 a.u.^{2}, which is in excellent agreement with the full potential linearized augmented plane wave (FLAPW) result (6.96 a.u.^{2} in Ref. 2).

[1] V. I. Anisimov *et al.*, Phys. Rev. B **71**, 125119 (2005).

[2] F. Lechermann, A. Georges, A. Poteryaev, S. Biermann, M. Posternak, A. Yamasaki, and O. K. Andersen, Phys. Rev. B **74**, 125120 (2006).

[3] V. I. Anisimov, A. I. Poteryaev, M. A. Korotin, A. O. Anokhin, and G. Kotliar, J. Phys.: Condens. Matter **9**, 7359 (1997).

[4] A. I. Lichtenstein and M. I. Katsnelson, Phys. Rev. B **57**, 6884 (1998).

[5] S. Y. Savrasov, G. Kotliar, and E. Abrahams, Nature (London) **410**, 793 (2001).

[6] O. K. Andersen, Phys. Rev. B **12**, 3060 (1975).

[7] E. Pavarini, S. Biermann, A. Poteryaev, A. I. Lichtenstein, A. Georges, and O. K. Andersen, Phys. Rev. Lett. **92**, 176403 (2004).

[8] O. K. Andersen and T. Saha-Dasgupta, Phys. Rev. B **62**, R16219 (2000).

[9] J. des Cloizeaux, Phys. Rev. **129**, 554 (1963).

[10] W. Ku, H. Rosner, W. E. Pickett, and R. T. Scalettar, Phys. Rev. Lett. **89**, 167204 (2002).

[11] N. Marzari and D. Vanderbilt, Phys. Rev. B **56**, 12847 (1997).

[12] M. Imada, A. Fujimori, and Y. Tokura, Rev. Mod. Phys. **70**, 1039 (1998).

[13] A. Fujimori, I. Hase, H. Namatame, Y. Fujishima, Y. Tokura, H. Eisaki, S. Uchida, K. Takegahara, and F. M. F. de Groot, Phys. Rev. Lett. **69**, 1796 (1992).

[14] K. Maiti, D. D. Sarma, M. Rozenberg, I. Inoue, H. Makino, O. Goto, M. Pedio, and R. Cimino, Europhys. Lett. **55**, 246 (2001).

[15] K. Maiti, Ph.D. thesis, IISC, 1997.

[16] I. H. Inoue, I. Hase, Y. Aiura, A. Fujimori, Y. Haruyama, T. Maruyama, and Y. Nishihara, Phys. Rev. Lett. **74**, 2539 (1995).

[17] A. Sekiyama *et al.*, Phys. Rev. Lett. **93**, 156402 (2004).

[18] A. Liebsch, Phys. Rev. Lett. **90**, 096401 (2003).

[19] I. A. Nekrasov, G. Keller, D. E. Kondakov, A. V. Kozhevnikov, T. Pruschke, K. Held, D. Vollhardt, and V. I. Anisimov, Phys. Rev. B **72**, 155106 (2005).

[20] E. Pavarini, S. Biermann, A. Poteryaev, A. I. Lichtenstein, A. Georges, and O. K. Andersen, Phys. Rev. Lett. **92**, 176403 (2004).

[21] T. Yoshida, K. Tanaka, H. Yagi, A. Ino, H. Eisaki, A. Fujimori, and Z.-X. Shen, Phys. Rev. Lett. **95**, 146404 (2005).

[22] H. Wadati, T. Yoshida, A. Chikamatsu, H. Kumigashira, M. Oshima, H. Eisaki, Z. X. Shen, T. Mizokawa, and A. Fujimori, Phase Transitions **79**, 617 (2006).

[23] I. V. Solovyev, Phys. Rev. B **73**, 155117 (2006).

[24] I. A. Nekrasov, K. Held, G. Keller, D. E. Kondakov, T. Pruschke, M. Kollar, O. K. Andersen, V. I. Anisimov, and D. Vollhardt, Phys. Rev. B **73**, 155112 (2006).

[25] R. Eguchi *et al.*, Phys. Rev. Lett. **96**, 076402 (2006).

[26] A. R. Tackett, N. A. W. Holzwarth, and G. E. Matthews, Comput. Phys. Commun. **135**, 329 (2001).

[27] N. A. W. Holzwarth, M. Torrent, and F. Jollet, ATOMPAW, 2007 (http://pwpaw.wfu.edu/).

[28] X. Gonze *et al.*, Comput. Mater. Sci. **25**, 478 (2002).

[29] M. Torrent, F. Jollet, F. Bottin, G. Zerah, and X. Gonze, Comput. Mater. Sci. **42**, 337 (2008).

[30] R. Frésard and G. Kotliar, Phys. Rev. B **56**, 12909 (1997).

[31] K. Maiti, U. Manju, S. Ray, P. Mahadevan, D. D. S. I. H. Inoue, and C. Carbone, Phys. Rev. B **73**, 052508 (2006).

[32] J. T. Sparks and T. Komoto, Phys. Lett. **25A**, 398 (1967).

[33] R. M. White and N. F. Mott, Philos. Mag. **24**, 845 (1971).

[34] T. Ohtani, K. Kosuge, and S. Kachi, J. Phys. Soc. Jpn. **28**, 1588 (1970).

[35] R. Benoit, J. Chem. Phys. **52**, 119 (1955).

[36] J. Trahan, R. G. Goodrich, and S. F. Watkins, Phys. Rev. B **2**, 2859 (1970).

[37] J. Zaanen, G. A. Sawatzky, and J. W. Allen, Phys. Rev. Lett. **55**, 418 (1985).

[38] L. Mattheiss, Phys. Rev. B **10**, 995 (1974).

[39] B. Meyer, C. Elsässer, F. Lechermann, and M. Fähnle, *FORTRAN 90 Program for Mixed-Basis-Pseudopotential Calculations for Crystals* (Max-Planck-Institut für Metallforschung, Stuttgart, in press).

[40] S. Hüfner, T. Riesterer, and F. Hulliger, Solid State Commun. **54**, 689 (1985).

[41] A. Fujimori, K. Terakura, M. Taniguchi, S. Ogawa, S. Suga, M. Matoba, and S. Anzai, Phys. Rev. B **37**, 3109 (1988).

[42] V. I. Anisimov, J. Zaanen, and O. K. Andersen, Phys. Rev. B **44**, 943 (1991).

[43] M. Nakamura, A. Sekiyama, H. Namatame, H. Kino, A. Fujimori, A. Misu, H. Ikoma, M. Matoba, and S. Anzai, Phys. Rev. Lett. **73**, 2891 (1994).

[44] M. Usuda and N. Hamada, J. Phys. Chem. **69**, 744 (2000).

[45] S. R. Krishnakumar, N. Shanthi, P. Mahadevan, and D. D. Sarma, Phys. Rev. B **61**, 16370 (2000).

[46] J. Kuneš, V. I. Anisimov, A. V. Lukoyanov, and D. Vollhardt, Phys. Rev. B **75**, 165115 (2007).

[47] J. Kuneš, V. I. Anisimov, S. L. Skornyakov, A. V. Lukoyanov, and D. Vollhardt, Phys. Rev. Lett. **99**, 156404 (2007).

[48] P. E. Blöchl, Phys. Rev. B **50**, 17953 (1994).

[49] S. G. Louie, K. M. Ho, and M. L. Cohen, Phys. Rev. B **19**, 1774 (1979).

[50] O. Bengone, M. Alouani, P. Blöchl, and J. Hugel, Phys. Rev. B **62**, 16392 (2000).

[51] B. Amadon, F. Jollet, and M. Torrent, Phys. Rev. B **77**, 155104 (2008).

[52] G. Kresse and J. Hafner, J. Phys.: Condens. Matter **6**, 8245 (1994).

[53] M. T. Czyżyk and G. A. Sawatzky, Phys. Rev. B **49**, 14211 (1994).

[54] A. Ferretti, A. Calzolari, B. Bonferroni, and R. D. Felice, J. Phys.: Condens. Matter **19**, 036215 (2007).

[55] A. A. Mostofi, J. R. Yates, Y.-S. Lee, I. Souza, D. Vanderbilt, and N. Marzari, Comput. Phys. Commun. **178**, 685 (2008).

[56] Dm. Korotin, A. V. Kozhevnikov, S. L. Skornyakov, I. Leonov, N. Binggeli, V. I. Anisimov, and G. Trimarchi, arXiv:0801.3500 (unpublished).